Quantitative Plane-Resolved Crystal Growth and Dissolution Kinetics by Coupling *In Situ* Optical Microscopy and Diffusion Models: the Case of Salicylic Acid in Aqueous Solution

Amelia R. Perry, Massimo Peruffo, and Patrick R. Unwin*

Department of Chemistry, University of Warwick, Gibbet Hill Road, Coventry, CV4 7AL, UK

E-mail: p.r.unwin@warwick.ac.uk

*To whom correspondence should be addressed

Abstract

The growth and dissolution kinetics of salicylic acid crystals are investigated *in situ* by focusing on individual microscale crystals. From a combination of optical microscopy and finite element method (FEM) modeling, it was possible to obtain a detailed quantitative picture of dissolution and growth dynamics for individual crystal faces. The approach uses real-time *in situ* growth and dissolution data (crystal size and shape as a function of time) to parameterize a FEM model incorporating surface kinetics and bulk to surface diffusion, from which concentration distributions and fluxes are obtained directly. It was found that the (001) face showed strong mass transport (diffusion) controlled behavior with an average surface concentration close to the solubility value during growth and dissolution over a wide range of bulk saturation levels. The ($\bar{1}10$) and (110) faces exhibited mixed mass transport/surface controlled behavior, but with a strong diffusive component. As crystals became relatively large, they tended to exhibit peculiar hollow structures in the end (001) face, observed by interferometry and optical microscopy. Such features have been reported in a number of crystals but there has not been a satisfactory explanation for their origin. The mass transport simulations indicate that there is a large difference in flux across the crystal surface, with high values at the edge of the (001) face compared to the center, and this flux has to be redistributed across the (001) surface. As the crystal grows, the redistribution process evidently can not be maintained so that the edges grow at the expense of the center, ultimately creating high index internal structures. At later times, we postulate that these high energy faces - starved of material from solution - dissolve and the extra flux of salicylic acid causes the voids to close.

Introduction

There is currently much interest in crystal growth and dissolution of both inorganic[1,2] and organic crystals.[3–5] Organic crystals are of particular interest in the pharmaceutical and food industries, where crystal structure, morphology and size impacts on usage. The study herein concerns salicylic acid (2-hydroxybenzoic acid or *o*-hydroxybenzoic acid), which has been used throughout history as a painkiller and anti-inflammatory, originally extracted from willow bark.[6,7] In modern medicine it is much more commonly seen in its esterified form, aspirin, although salicylic acid itself is used to treat various skin ailments. Despite these important uses, the crystallization and dissolution kinetics of salicylic acid have not been investigated extensively. The investigations we report herein are aimed at providing considerable new information on the growth and dissolution of individual crystals of salicylic acid at a level where the behavior of each exposed crystal face can be determined. Furthermore, the methodology described should be of widespread utility and general interest.

A range of imaging methods have been proposed to address crystal growth and dissolution at the level of an individual crystal face.[8] Phase shift interferometry (PSI),[9,10] atomic force microscopy (AFM)[11–13] and confocal microscopy[14] have all been used to investigate the kinetics of crystal growth.[15] However, for salicylic acid, only dissolution kinetics have been investigated using *in situ* AFM.[16–18] In water, the (110) and ($\bar{1}$10) faces were studied[16] and dissolution rates determined.

The most common type of investigation of crystal growth and dissolution involves batch stirring systems where bulk rates are measured over time.[19–21] While such systems provide some insights into crystal growth kinetics, data are averaged over a range of different crystal sizes, and exposed crystal faces. Furthermore, although mass transport correlations are available for such suspensions,[24] they are rather crude which makes it difficult to precisely separate mass transport and surface kinetic effects. Salicylic acid crystal growth has been studied and modeled using such approaches.[20–23] Blandin *et al.*[20] proposed that the growth of salicylic acid crystals is diffusion controlled at low supersaturations, as did Nallet *et al.*[21]

The mechanism of crystal growth and dissolution can be understood in terms of two processes: the diffusion of species between the bulk solution and the surface of the crystal; and movement of species at the crystal surface including surface diffusion, integration, and the adsorption and desorption of crystal growth units. Herein, the situation where the former process is slow compared to any surface phenomena is described as mass transport (diffusion) controlled, whereas a surface kinetic limitation is described as surface controlled.

Quantitative methods which examine micro-crystals are valuable because of the many and varied applications of crystals on this scale, as highlighted briefly above. Furthermore, as we show herein, micro-crystals are easier to fully characterize (i.e. to determine the reactivity of individual exposed crystal planes). Moreover, if isolated, micro-crystals are subject to a well-defined mass transport (diffusion) regime, as exemplified by electrochemical studies of ultramicroelectrodes (UMEs).[25,26] Put simply, just as reducing the size of a voltammetric/amperometric UME enhances the diffusion rate (magnitude proportional to the inverse of the characteristic electrode dimension[25]), so does shrinking the size of an isolated crystal. Thus, as we show in this paper, one can promote well-defined (and high) diffusion rates by studying microscale crystals. This enhances the opportunity to observe the influence of surface kinetics in heterogeneous physicochemical processes. Herein, we visualize the growth and dissolution of micro-crystals *in situ* and use the experimental data obtained as parameters for a finite element model that then reveals the kinetic regime. The importance of diffusion compared to surface reactions in determining the reactivity is revealed, and the approach allows concentration distributions around growing and dissolving crystals to be predicted.

A further consideration in the growth and dissolution of salicylic acid is polymorphism.[27–29] Nordström *et al.*[30] have shown that for salicylic acid crystals formed from aqueous solution, there is only one polymorph, but that the crystals often produced 'peculiar, hollow tubes with square cross sectional areas' as well as simple needle structures. Blandin *et al.*[20] describe the crystals as 'prismatic needle or rod shaped'. Xu *et al.*[31] have described four different morphologies of salicylic acid crystallites when prepared in the presence of four different modifiers.

There is a fairly limited body of work on hollow crystals[32,33] and the mechanism of their formation has not clearly been established, although it has been postulated that the presence of hollow features is due to dislocations.[34] In the present study, hollow features in salicylic acid crystals were sometimes observed, and the mass transport simulations that are an integral part of our studies provide key insights into the conditions under which hollow features appear. Trapped bubbles which result may be a concern for producing crystalline drug forms, and studies such as those described herein could be used to set conditions under which these undesirable features could be avoided.

Experimental

Solutions and Samples All solutions were prepared using ultrapure water (Milli-Q Reagent, Millipore) with a typical resistivity of 18.2 M Ω cm at 25 $^{\circ}$C.

Seed micro-crystals were produced on 47 mm diameter circular glass microscope slides (Thermo Scientific), that had been cleaned with acetone (Sigma, $> 99.5\%$) and then blown dry using nitrogen gas (BOC). They were then assembled into petri dishes (Willco Wells) equipped with a perspex rim and lid. The surface of the slides was functionalized with a thin film of poly-$_{\mathrm{L}}$-lysine (PLL) which provided a surface for the nucleation of well-defined micro-crystals. The PLL film was prepared using 1 mg ml^{-1} PLL (Sigma) solution that was pipetted into the petri dishes to cover the slide and left to develop for 30 minutes. The slides were then washed with ultrapure water and blown dry using nitrogen.

Micro-crystals were produced using 3 ml each of 37.5 mM sodium salicylate (Sigma, $> 99.5\%$) and 90 mM sulfuric acid (Sigma, $> 95\%$) pipetted into the PLL-functionalized petri dishes, mixed and left stationary for 45 minutes in order to nucleate micro-crystals on the surface. The petri dish containing the micro-crystals was rinsed with water and dried using nitrogen.

This method successfully produced a surface with crystals with a typical largest dimension of 40-80 μm. The crystals produced were usually orientated with the (110) plane perpendicular to

the glass surface, as shown in Figure 1. The salicylic acid crystals had a tabular morphology, as shown. The unit cell, as described by Cochran,[35] and further refined by Sundarlingham *et al.*[36] is monoclinic, but almost tabular.

Crystal Growth Investigations 3 ml of sodium salicylate (of a defined concentration in the range 14-30 mM) and 3 ml of 60 mM 'sulphuric acid were pipetted and mixed in a petri dish containing the micro-crystals. A 40× dipping lens on a Leica DM4000 M compound microscope was lowered into the solution and a suitably isolated micro-crystal was located such that the nearest crystal on the surface of the slide was at a distance of at least 30× the largest dimension of the crystal. The lateral resolution was ca. 0.5 μm. This ensured that the micro-crystal investigated was essentially diffusionally isolated for the purpose of crystal growth rate analysis.

A time sequence of images was taken for a particular crystal, typically every 30 s for a duration of one to two hours. Examples of time sequences for dissolution and growth are shown in Figure 2, which highlight how the crystal dimensions change over time. From the time lapse sequence, the expansion or contraction of the (001) and ($\bar{1}$10) faces of the crystal (see Figure 1) were measured directly with the aid of ImageJ (Version 1.45, NIH).

Simulations and Modeling

Salicylic acid solution in the presence of the solid (crystal) phase is characterized mainly by the following equilibria:

$$\mathrm{Sal}^{-}_{(\mathrm{aq})} + \mathrm{H}^{+}_{(\mathrm{aq})} \underset{k_b}{\overset{k_f}{\rightleftharpoons}} \mathrm{HSal}_{(\mathrm{aq})} \tag{1}$$

$$\mathrm{HSal}_{(\mathrm{aq})} \rightleftharpoons \mathrm{HSal}_{(\mathrm{s})} \tag{2}$$

where Sal^{-} represents the salicylate ion and HSal is salicylic acid.

Speciation in the solution was calculated using MINEQL^{+} (Environmental Research Software,

version 4.6), which also allowed the ionic strength and pH of the solution to be calculated. The program uses the Davies equation[37] to estimate activity coefficients. The temperature was set to the experimental value of 22 °C. The pK_a of salicylic acid was taken from literature as 2.98.[38]

Finite element modeling was performed using Comsol Multiphysics 4.2a (Comsol AB, Sweden) using a Dell Intel core 7i Quad 2.93 GHz computer equipped with 16 GB of RAM running Windows 7 Professional $\times$64 bit. The basic geometry for the model is shown in Figure 3. Simulations were carried out with $>$ 12,000 tetrahedral mesh elements. The mesh resolution was defined to be finest near the surface of the crystal (close to boundaries 1, 2 and 3). Simulations of varying mesh density were performed to ensure that a fine enough mesh was used for the model calculations reported herein. Boundaries 4 and 5 are planes of symmetry, as defined earlier.

The three inter-dependent species Sal^-, H^+ and HSal (Equation 1) were considered in the model. For the experimental length scale, mass transport is predominantly controlled by diffusion, for which the following equation was solved:

$$D_j \nabla^2 c_j + R_j = 0 \tag{3}$$

where D_j is the diffusion coefficient, c_j is the concentration and j is the species of interest. R_j is a kinetic term representing the the loss and/or formation of species j according to Equation 1 which is always at equilibrium. The diffusion coefficients of the individual species can be considered to be constant over the spatial domain investigated: $D_{Sal^-} = D_{HSal} = 8.4 \times 10^{-10}$ m^2 s^{-1} [39] and $D_{H^+} = 7.6 \times 10^{-9}$ m^2 s^{-1}.[40]

The boundary conditions applied to the model can be understood with reference to Figure 3. Boundaries labeled 1, 2 and 3, representing the growing or dissolving crystal faces, had experimentally determined fluxes of salicylic acid imposed. Thus, the equations satisfied on these boundaries are as follows:

$$\text{boundary 1: } \mathbf{n}.(D_{HSal} \nabla c_{HSal}) = -J_{(001)} \tag{4}$$

$$\text{boundary 2: } \mathbf{n}.(D_{\text{HSal}}\nabla c_{\text{HSal}}) = -J_{(\bar{1}10)} \tag{5}$$

$$\text{boundary 3: } \mathbf{n}.(D_{\text{HSal}}\nabla c_{\text{HSal}}) = -J_{(110)} \tag{6}$$

where $J_{(001)}$, $J_{(\bar{1}10)}$ and $J_{(110)}$ define the flux of HSal incorporated into the (001), ($\bar{1}$10) and (110) face, respectively, and **n** is the inward unit vector normal to the boundary. Note that we only needed to consider HSal and not the individual ions at the boundary itself because a rapid equilibrium between H^+, Sal^- and HSal is reasonably assumed (on the timescale of the diffusion process). For computational efficiency we made use of symmetry planes denoted by boundaries 4 and 5, which have no-flux boundary conditions, so that just one quarter of a crystal is simulated. Boundary 6 is constrained by a no-flux condition, to represent the unreactive glass slide on which the crystal grows. Hence:

$$\text{boundary 4-6: } \mathbf{n}.(D_j\nabla c_j) = 0 \tag{7}$$

Boundaries 7-9 are set by a bulk concentration condition, because they are a considerable distance away from the crystal to be considered as bulk solution (typically at least 40 times the largest dimension of the crystal in the simulation). We may reasonably write:

$$\text{boundary 7-9: } c_j = c_{bulk,j} \tag{8}$$

where $c_{bulk,j}$ is the bulk concentration of $j = Sal^-$, HSal and H^+. The pH values calculated from MINEQL$^+$, which were consistent with those measured experimentally, were used to calculate $c_{bulk,\text{HSal}}$. The concentration of the protonated and unprotonated salicylate were calculated from the acid dissociation constant K_a (see above; corrected for ionic strength) and the total concentration of the two species HSal_{tot} (known from the dissolved quantity of sodium salicylate).

The reaction rates in Equation 3 were calculated based on the equilibrium in Equation 1 with

the ratio fixed by the acid dissociation constant:

$$K_a = \frac{k_f}{k_b} \tag{9}$$

and rate constants sufficiently high to maintain equilibrium at all points in solution.

Results and discussion

Characterization of Salicylic Acid Micro-crystals The orientation of crystals, typically represented by that in Figure 1, was determined by powder X-ray diffraction (XRD, not reported), to elucidate that the (110) face of the micro-crystal was usually parallel with the glass surface. The other two faces were determined from this result, guided by literature,[17,18] and the known crystal structure.[35,36]

The 2-dimensional *in situ* data from optical microscopy, which determined growth/dissolution of the (001) and ($\bar{1}$10) faces, were combined with information from vertical scanning interferometry (VSI) to determine the height, in order to provide 3-D growth rates of crystals, needed for FEM simulations. For this purpose, samples were produced as described previously and then sputtered with a layer of gold of approximately 10 nm. Interferometry images were obtained for a range of crystals with dimensions of 50-250 μm. It was deduced that the height, h, of the crystals was related to the width, w, by $h = 0.76(\pm 0.3)w$.

Determination of *In Situ* Crystal Growth Rates and Interfacial Concentrations Plots of the displacement of the (001) and ($\bar{1}$10) faces over time were produced from *in situ* optical microscopy for crystal growth and dissolution. Typical example plots in Figure 4 show the expected features of a shrinking crystal for dissolution and expanding planes for crystal growth. It is evident that the (001) plane is much more active than the ($\bar{1}$10) face for both dissolution and growth. It is also clear from the long time plots (4a and c) that although the growth and dissolution rate of the crystal is close to linear with time, the relationship is not strict, especially for the (001) face,

where the apparent growth rate evidently decreases at longer times for growth (corresponding to increased crystal size) and increases at longer times for dissolution (decreased crystal size). This can be attributed to the influence of mass transport, because diffusion rates alter as the micro-crystal dimension changes with time. In brief, diffusion rates to micro-scale interfaces scale with the inverse of the characteristic dimension.[25] This effect does not seem to be as evident in the growth and dissolution behavior of the $(\bar{1}10)$ face.

For quantitative analysis, we focused on growth over relatively short times (as indicated, for example, to the right of Figure 4). For shorter periods of time, where the overall crystal dimensions change less, a close to linear relationship between crystal dimensions and time is evident. A static FEM model, relevant to the crystal size for the time period of interest, could be used to analyze mass transport and crystal reactivity, because the characteristic diffusion time of the experimental micro-crystal system was much faster than that for changes in crystal dimensions by growth and dissolution. This resulted in considerable computational efficiency compared to an equivalent time-dependent moving boundary model.

The flux $J_{(xyz)}$ of salicylic acid was determined for each face (xyz) of the crystal from:

$$J_{(xyz)} = v_{(xyz)}\rho_{\mathrm{HSal}} \tag{10}$$

where $v_{(xyz)}$ is the experimentally determined growth or dissolution velocity of face (xyz) and ρ_{HSal} is the molar volume of salicylic acid, calculated from the density of salicylic acid (1.443 g cm^3 [41]).

Figure 5 shows the relationship between flux into or out of the two characteristic crystal faces as a function of the bulk solution concentration. The saturation ratio of the solution is given by:

$$S = \frac{c_{bulk,\mathrm{HSal}}}{c^*_{bulk,\mathrm{HSal}}} \tag{11}$$

where $c^*_{bulk,\mathrm{HSal}}$ is the concentration in bulk when there is neither dissolution or growth. This is determined by the intercept on the y axis in Figure 5. When $S \geq 1$ the system is supersaturated,

meaning that crystal growth occurs, and when $S < 1$ the crystal will dissolve. In equilibrium, the bulk solution concentration (of fully protonated salicylic acid) at $S = 1$ are as follows for the (001) face and the $(\bar{1}10)$ faces, $c^*_{(001),bulk,\mathrm{HSal}}$ and $c^*_{(\bar{1}10),bulk,\mathrm{HSal}}$, respectively:

$$c^*_{(001),bulk,\mathrm{HSal}} = 10.0^{+}_{-}0.5 \text{ mM} \tag{12}$$

$$c^*_{(\bar{1}10),bulk,\mathrm{HSal}} = 10.3^{+}_{-}0.6 \text{ mM} \tag{13}$$

We notice that these values are similar, but slightly lower than the solubility of salicylic acid previously reported in literature. Nordström *et al.*[30] found that the solubility of salicylic acid was 11.6 mM at 20°C in water. Compton *et al.*[17] report a solubility of 14.9 mM for total salicylic acid and salicylate, which is equal to a value of 11.2 mM for just the salicylic acid species.

It is important to comment on the noticeable range in measured flux at each bulk concentration in Figure 5. This is largely due to the range of crystal sizes studied and the fact that the crystals grow and dissolve with a significant contribution of diffusion, which then has a major influence on the flux. Thus, while the composite plot in Figure 5 identifies general trends, the growth and dissolution behavior of individual crystals was examined to extract kinetics using FEM simulations to mimic the precise crystal dimensions.

Typical example outputs of the FEM simulations for dissolution and growth are shown in Figure 6. For the case of growth the bulk concentration was 11.2 mM and for dissolution it was 8.4 mM and the crystal dimensions are indicated in the caption. During dissolution (Figure 6a) the salicylic acid concentration close to the crystal surface is higher than in the bulk solution, and there is evidently a concentration boundary layer (or diffusion layer) from the crystal to the bulk. This is particularly pronounced for the (001) face.

For the case of growth (Figure 6b), the simulations show broadly similar trends for the concentration on the faces, but with the crystal acting as a sink for salicylic acid. The concentration is now lower on the faster growing (001) face. Again, on the other faces, the concentration profile

from the crystal to the bulk is less pronounced.

Figure 7 shows the concentration profiles perpendicular to the center of the three crystal faces, for the cases of dissolution and growth shown in figure 6. This clearly shows that the crystal faces act as sinks and sources of salicylic acid to different degrees. Close to the crystal the gradient is steeper for the (001) surface (for dissolution and growth), as expected based on the optical microscopy data. The difference between the surface concentrations of salicylic acid on the (110) and ($\bar{1}$10) faces for dissolution and growth indicates that although there is a significant mass transport component during dissolution and growth of these faces, there is some surface kinetic control. For the (001) face the surface concentrations are closer to those for a purely transport-controlled system. In fact, these surface concentrations cross over so that the value for growth is lower than for dissolution. This is not expected to be a real effect, but rather associated with the difficulty of precisely determining crystal dimensions and particularly measuring the morphology of dissolving crystals due to pitting. The fuzzy crystal outlines (see Figure 2a, for example) introduced a small systematic error defining the crystal surface, which tended to cause a slight underestimation of the crystal dimensions.

For the (001) face in the growth regime ($c_{bulk,\mathrm{HSal}} > 10$ mM), the concentration does not change appreciably with bulk concentration, and attains values close to the saturated value. This indicates clearly that growth of this face is dominated by diffusion. In contrast, the ($\bar{1}$10) and (110) faces both show a small, systematic increase in the surface concentration with increased bulk concentration. However, concentration values are much lower than the bulk concentration, indicative of small, but detectable, contribution of surface kinetics to the overall rate, consistent with the arguments presented above. In the dissolution regime, all faces appear to show a small amount of surface kinetic control, but there is still a strong diffusion component. We note that there is a perhaps a slight overestimate of the dissolution rate, reflected in higher surface concentrations, due to pitting of the crystal during dissolution, which makes it difficult to define the crystal size, as discussed above in relation to Figure 2a. However, this does not prevent us from semiquantitavely identifying the main trend.

As highlighted earlier, there has been little investigation into the growth and dissolution of salicylic acid, but it is informative to compare our results to prior work, where quantitative comparisons can be made. Compton *et al.*[16,17] investigated the dissolution kinetics of large, exposed (110) and ($\bar{1}$10) faces of salicylic acid (typically $3 \times 3 \times 30$ mm), using a hydrodynamic AFM flow cell to measure the dissolution rate. For the ($\bar{1}$10) face with bulk concentrations of total dissolved salicylic acid of 0 mM, 3 mM and 10 mM they concluded that the dissolution process was surface-controlled with a surface flux of the order 10^{-5} mol cm^{-2} s^{-1},[16] while we observed for the same faces a dominant mass transport component with comparable or higher fluxes for similar saturation levels. They measured the overall retreat of the surfaces as small changes in the mean height; such measurements are extremely sensitive to drift of the piezoelectric controller,[42] and requires very careful surface control if the accuracy of AFM dissolution studies is to be compromised.[43] Moreover, in Figure 10,[17] the data for 7 mM and water could arguably just as easily be linearly fitted to the mass transport rate. We also note that a significant dissolution rate was reported for a saturated solution in these studies, whereas no net dissolution would be expected.

Hollow Features in Crystals When larger dimensions (50-100 μm width) were achieved, the crystals were often found to exhibit hollow features in the (001) face. Example bright field microscopy images of such crystals are illustrated in Figure 9a. Confirmation of holes in the crystal was achieved by VSI measurements, such as the data shown in Figure 9b and c. It is evident that the hollow features extend in these cases about 100 μm into the body of the crystals.

We can explain and rationalize the formation of these hollow features in terms of mass transport control which dominates the large micro-crystals (*vide supra*). Figure 10 compares the growth of the two (001) end planes of salicylic acid micro-crystals, labeled A and B (below the plot), with respect to a common reference plane shown by the dashed line across the center of the crystal images. In the B direction, considerable hollow features are observed in the crystal during the time period shown, whereas in the A direction, the (001) face is flat and does not appear to show any of these characteristic holes. For this time period there is a noticeable difference between the growth

rates observed in the A and B directions. The crystal grows more quickly in the B direction with an average growth rate of 0.075($\pm$0.006) μm s^{-1} compared to 0.047($\pm$0.006) μm s^{-1} in the A direction. This is because the active area at the end of the B face is smaller and so recieves a high diffusive flux of material.

We see from simulations (e.g. Figure 6b) that during growth on the (001) face, the flux is higher at the edge of the face (steeper concentration gradient) than in the center of the face. In contrast, growth of the (110) and ($\bar{1}$10) faces is under mixed diffusion/surface kinetic control. This picture of mass transport is shown schematically in Figure 11a. Because the (001) face is flat, but grows at a diffusion limited rate, the near interface concentration of salicylic acid has to be at the saturated level and to maintain a uniform growth rate of the surface, material has to be redistributed across the face (e.g. by surface diffusion). The larger the crystal, the greater the distance which the material has to diffuse from the edge to the center, and it is evident that a point is reached where this cannot be sustained so that HSal is incorporated at the edges faster than at the center. At this stage (Figure 11b) the edges of the (001) face start to grow preferentially, depleting material and slowing growth at the center. Moreover, the availability of HSal in solution at the edges compared to the center causes the edge to overgrow (Figure 11c). This process continues for a significant time, but an interesting aspect is that the hollows eventually close over. We postulate that the inner leading edge created inside the hollow feature (Figure 11d) would be expected to be of higher energy (higher solubility) and as this region is recessed it is starved of growth material. Thus, the leading edge could start to dissolve, with diffusion from the inner leading edge toward the edges, therefore closing the hollow. Interestingly, and supporting this hypothesis, the higher mass transport on the edges of the (001) face leads to a slightly convex morphology during dissolution (Figure 2a).

In previous literature, hollow features have been observed when crystals are produced by vapor deposition,[32] but little work on hollow crystals in solution has been carried to date. There has been some attempt at explaining the emergence of this phenomenon. It has been suggested that the origin of a hollow feature is a dislocation in the crystal structure,[34] with a spiral dislocation

being responsible for a pyramidal hollow like those observed in the present study for salicylic acid crystals.[44,45] The that data from FEM simulations show that the characteristic patterns of diffusive mass transport also appear to play a role in the emergence, growth and closure of hollow features.

Conclusions

This study has shown that time lapse optical microscopy combined with FEM modeling is an effective approach for probing micro-crystal growth and dissolution kinetics. In particular, using data from optical microscopy to parameterize a FEM model of a growing/dissolving crystal reveals direct information about concentration distribution around a crystal and the interfacial concentrations. This, in turn, allows the importance of diffusion compared to surface kinetics to be elucidated for each crystal face. For salicylic acid, the (001) face has been shown to be dominated by mass transport for both dissolution and growth, whereas the (110) and ($\bar{1}$10) faces show more surface kinetic control, although diffusion remains a significant component of the overall kinetics.

Knowledge of the importance of mass transport for this system has allowed a convincing explanation for the presence of hollow features seen when the crystals become large. These features are a direct consequence of differential flux across the (001) face with the edges experiencing a much higher diffusive flux than the center position. Ultimately this leads to preferred growth at the edges compared to the center, causing the formation of a hollow feature in this face. Interestingly, as time proceeds, these features become enclosed, with a roof structure. This suggests that the internal walls of the hollow feature (high index faces) become shielded from the growth flux that they dissolve so that the feature becomes enclosed. Hollow features have been seen in other micro-crystal systems and differential diffusive fluxes appear to provide a satisfactory analysis of this phenomenon.

Acknowledgement

We thank the European Research Council (ERC-2009-AdG247143-QUANTIF) for support of M. P. and P. R. U.; A. R. P. was supported by the UK Engineering and Physical Sciences Research Council.

References

(1) Gower, L. B. *Chem. Rev.* **2008**,108, 4551-4627

(2) De Yoreo, J. J.; Vekilov, P. G. *Rev. Min. Geochem.* **2003**, 54, 57-93

(3) Shekunov, B.Y.; York, P. *J. Pharm. Sci.* **2000**, 211, 122-136

(4) Shekunov, B. Y.; Chattopadhyay, P.; Tong, H. H. Y.; Chow, A. H. L. *Pharm. Res.* **2007** 24, 203-227

(5) Chen, J.; Sarma, B.; Evans, J. M. B.; Myerson, A. S. *Cryst. Growth Des.* **2011** 11, 887-895

(6) Chrubasik, S.; Eisenberg, E.; Balan, E.; Weinberger, T.; Luzzati, R.; Conradt, C. *Am. Journ. of Med.* **2000**, 109, 9-14

(7) Chrubasik, S.; Künzel, O.; Black, A.; Conradt, C.; Kerschbaumer, F. *Phytomed.* **2001**, 8, 241-251

(8) Unwin, P. R.; Macpherson, J. V. *Chem. Soc. Rev.* **1995**, 24, 109-119

(9) Onuma, K.; Kameyama, T.; Tsukamoto, K. *Cryst. Growth* **1994**, 137, 610-622

(10) Vekilov, P. G.; Kuznetsov, Y. G.; Chernov, A. A. *Cryst. Growth* **1992**, 121, 643-655

(11) Danesh, A.; Connell, S. D.; Davies, M. C.; Roberts, C. J.; Tendler, S. J. B.; Williams, P. M.; Wilkins, M. J. *Pharm. Res.* **2001**, 18, 3, 299-303

(12) Dobson, P. S.; Bindley, L. A.; Macpherson, J. V.; Unwin, P. R. *Langmuir* **2005**, 21, 1255-1260

(13) Vavouraki, A. I.; Putnis, C. V.; Koutsoukos, P. G. *Cryst. Growth Des.* **2010**, 10, 1, 60-69

(14) Shenoy, D. B.; Sukhorukov, G. B. *Euro. Pharma. Biopharma* **2004**, 58, 521-527

(15) Van Driessche, A. E. S.; Otalora, F.; Sazaki, G.; Sleutel, M.; Tsukamoto, K.; Gavira, J. A. *Cryst. Growth Des.* **2008**, 8, 12, 4316-4323

(16) Coles, B. A.; Compton, R. G.; Suárez, M.; Booth, J.; Hong, Q.; Sanders, G. H. W. *Langmuir* **1998**, 14, 218-225

(17) Wilkins, S. J.; Coles, B. A.; Compton, R. G.; Cowley, A. *J. Phys. Chem. B* **2002**, 106, 4763-4774

(18) Wilkins, S. J.; Suárez, M. F.; Hong, Q.; Coles, B. A.; Compton, R. G.; Tranter, G. E.; Firmin, D.; *J. Phys. Chem. B* **2000**, 104, 1539-1545

(19) De Anda, J. C.; Wang, X. Z.; Roberts, K. J. *Chem. Eng. Sci.* **2005**, 60, 1053-1065

(20) Blandin, A. F.; Mangin, D.; Nallet, V.; Klein, J. P.; Bossoutrot, J. M. *Chem. Eng. Journ.* **2001**, 81, 91-100

(21) Nallet, V.; Mangin, D.; Klein, J. P. *Chem. Eng.* **1998**, 22, 649-652

(22) Franck, R.; David, R.; Villermaux, J.; Klein, J. P. *Chem. Eng. Sci.* **1988**, 43, 1, 69-77

(23) Tavare, N. S.; Gaikar, V. G. *Ind. Eng. Chem. Res.* **1991**, 30, 722-728

(24) Briançon, S.; Colson, D.; Klein, J. P. *Chem. Eng.* **1998**, 70, 55-64

(25) Bard, A. J.; Faulkner, L. R *Electrochemical Methods, Fundamentals and Applications* John Wiley & Sons, New York **2001**

(26) Subero-Couroyer, C.; Mangin, D.; Rivoire, A.; Blandin, A. F.; Klein, J. P. *Powder Tech.* **2006**, 161, 98-109

(27) Haleblian, J.; McCrone, W. *J. Pharm. Sci.* **1969**, 58, 911-929

(28) Land, T. A.; Martin, T. L.; Potapenko, S.; Tayhas Plamore, G.; De Yoreo, J. J. *Nature* **1999**, 399, 442-445

(29) Mukata, T.; Lee, A. Y.; Kawakami, T.; Myerson, A. S. *Cryst. Growth Des.* **2005**, 5, 4, 1429-1436

(30) Nordström, F. L.; Rasmuson, A. C. *J. Chem. Eng. Data* **2006**, 51, 1668-1671

(31) Xu, Y.; Yin, H.; Lu, Y.; Yin, S.; Wu, H.; Jiang, T.; Wada, Y. *Mat. Let.* **2006**, 60, 2873-2876

(32) Simov, S. *Journ. Mat. Sci.* **1976**, 11, 2319-2332

(33) Natarajan, V.; Subramanian, C.; Ramasamy, P. *Journ. Mat. Sci. Letters* **1988**, 7, 511-512

(34) Chandrasekharaiah, M. N.; Krishna, P. *J. Cryst. Growth* **1969**, 5, 213-215

(35) Cochran, W. *Acta Cryst.* **1953**, 6, 260-268

(36) Sundarlingham, M.; Jensen, L. H. *Acta Cryst.* **1965**, 18, 1053-1058

(37) Davies, C.W. *Ion Association* London, Butterworths. **1962**, 37ï£¡53.

(38) Christensen, J. C.; Hansen, A. N. D.; Izatt, R. M. *title* Wiley-Interscience, New York **1976**

(39) Polakovic, M.; Gorner, T.; Villiéras, F.; de Donato, P.; Bersillon, J. L. *Langmuir* **2005**, 21, 7, 2988-2996

(40) Compton, R. G.; Unwin, P. R. *Phil. Trans. R. Soc. Lond.* **1990**, A330, 1-45.

(41) Lide, D.R. *CRC Handbook of Chemistry and Physics 86th Ed.*, CRC Press, **2005-2006**, 3-288

(42) Kim, J.; Shen, M.; Nioradze, N.; Amemiya, S. *Anal. Chem.* **2012**, 84, 3489-3492

(43) Clifford, C. A.; Seah, M. P. *Meas. Sci. Technol.* **2009**, 20

(44) Amleinckx, S. *Phil. Mag.* **1953**, 44, 337

(45) Nabarro, F. R. N. *Theory of Crystal Dislocation*, Oxford University Press, **1967**, 311

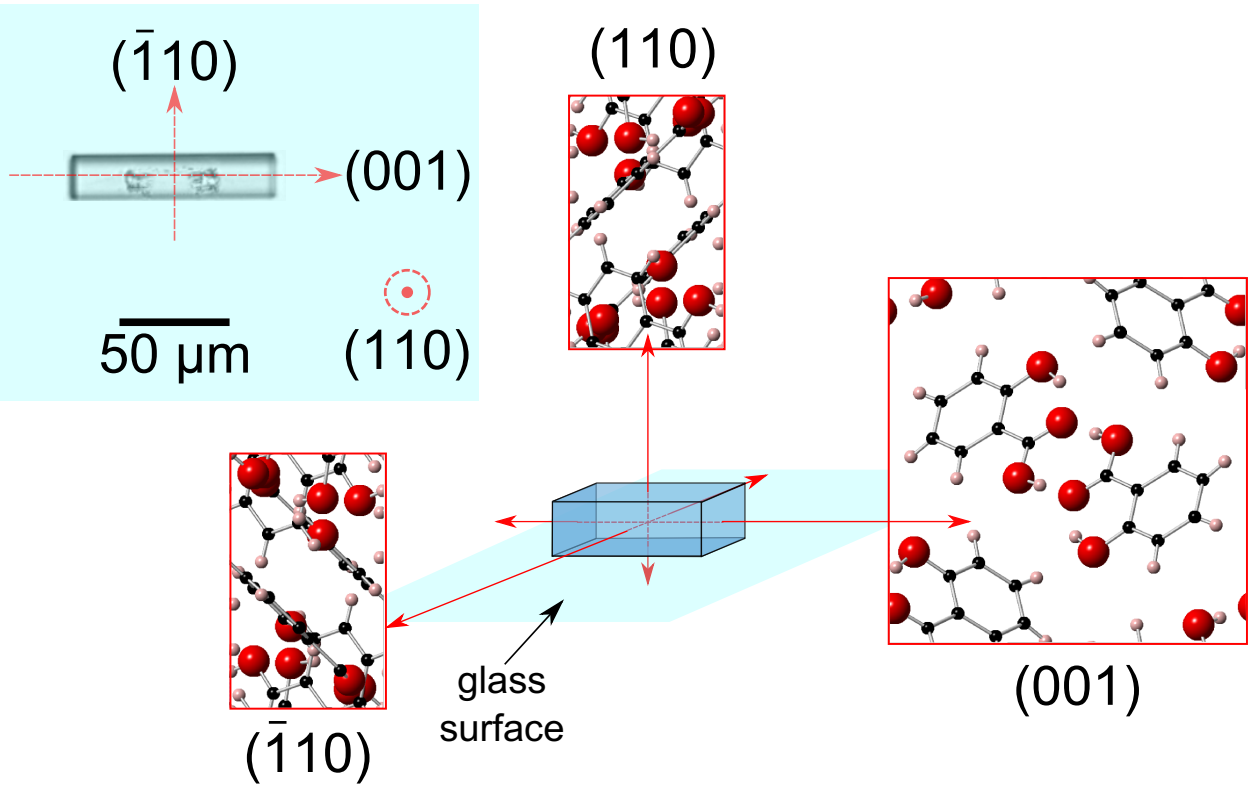

Figure 1: Morphology of the salicylic acid crystals. A 3d representation of the morphology with the defining exposed crystal planes labeled, and a bright field microscopy image (top left) of a typical salicylic acid crystal, with the corresponding planes shown.

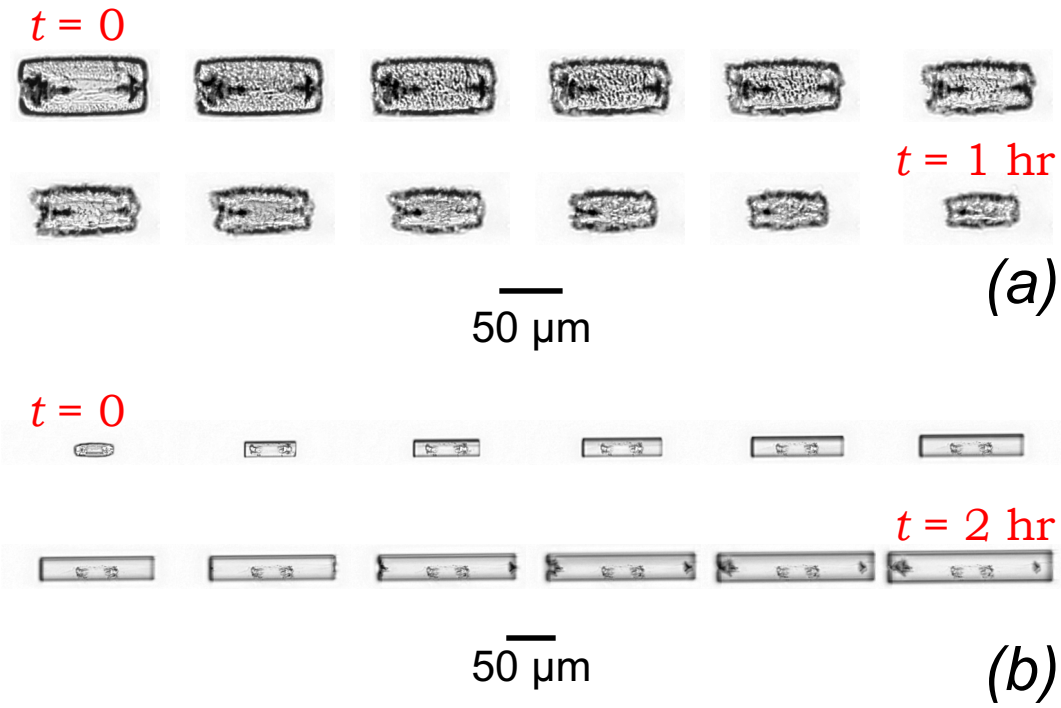

Figure 2: Time sequences for crystals during (a) dissolution over a period of 1 hour and (b) growth over a period of 2 hours, taken using optical microscopy. Dissolution is shown in a solution of 8.4 mM salicylic acid and growth is shown for the case of 13.0 mM salicylic acid.

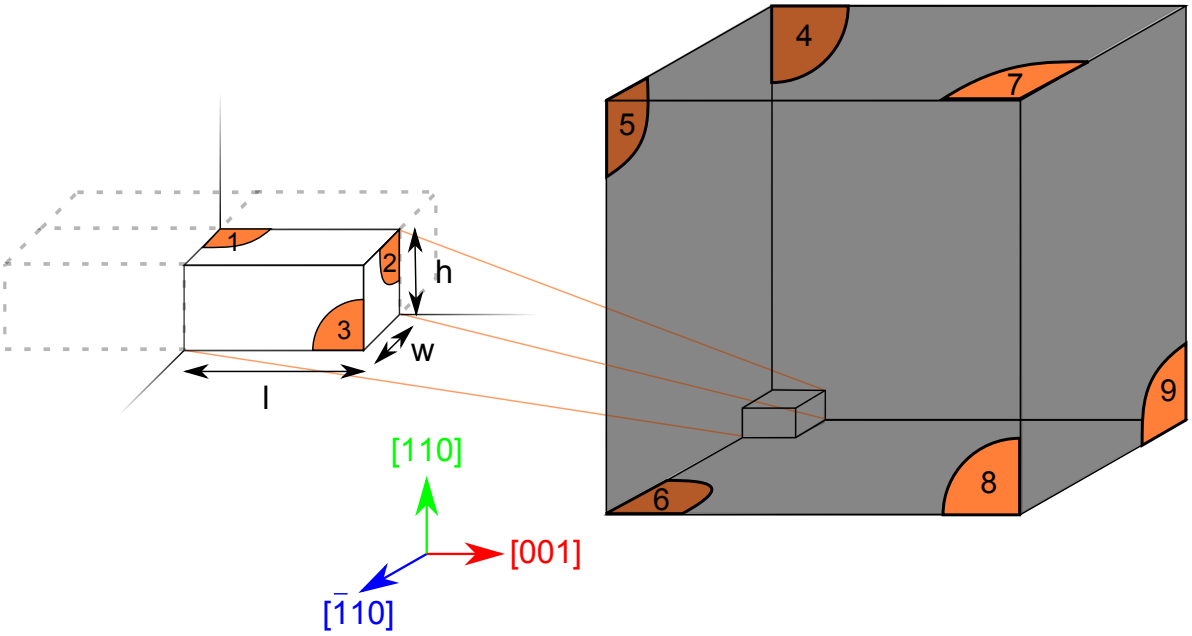

Figure 3: Model showing one quarter of the crystal (left), making use of two planes of symmetry to increase computational efficiency. The bulk solution consists of a cube with a dimension of $30l$, and the crystal dimensions are as follows; l is half of the crystal size along the [001] direction (the length), w is half of the crystal size along the [$\bar{1}$10] direction (the width), and h is the crystal size in the [110] direction (the height). The boundary conditions applied to the labeled faces are detailed in the text.

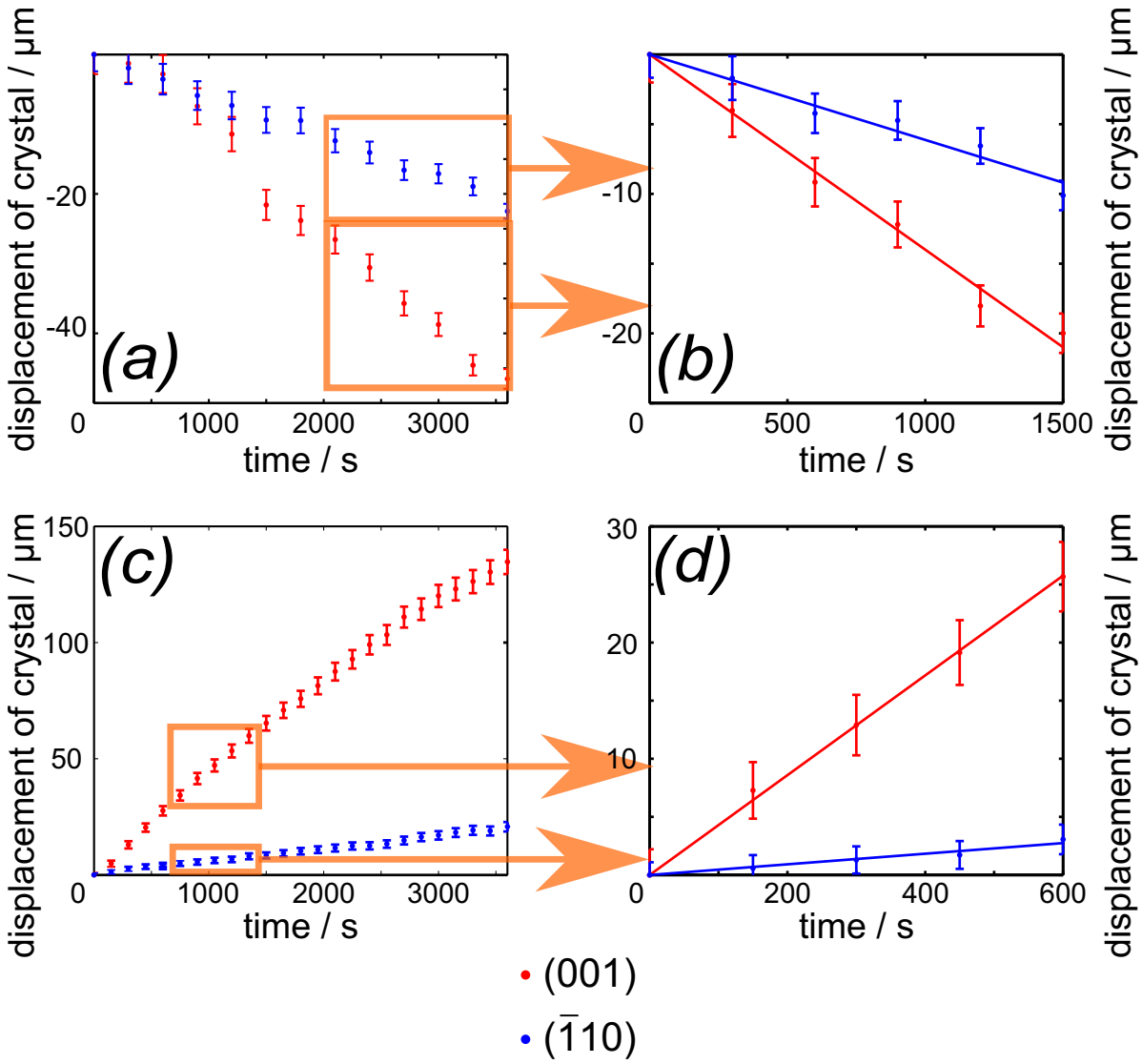

Figure 4: Plots showing the change in size of the two crystals in Figure 2 over time. Dissolution of a salicylic acid crystal (top) with average dimensions 56.5×23 μm in a solution of sodium salicylate concentration 8.4 mM. Growth of a salicylic acid crystal (bottom) with average dimensions 166.5×32 μm in a solution of salicylic acid concentration 13.0 mM. The plots on the left hand side correspond to the entire dissolution/growth period recorded and the graph on the right hand side corresponds to a short period of time of this experiment, as illustrated. Over a shorter period of time a constant dissolution/growth rate is observed for a particular solution composition.

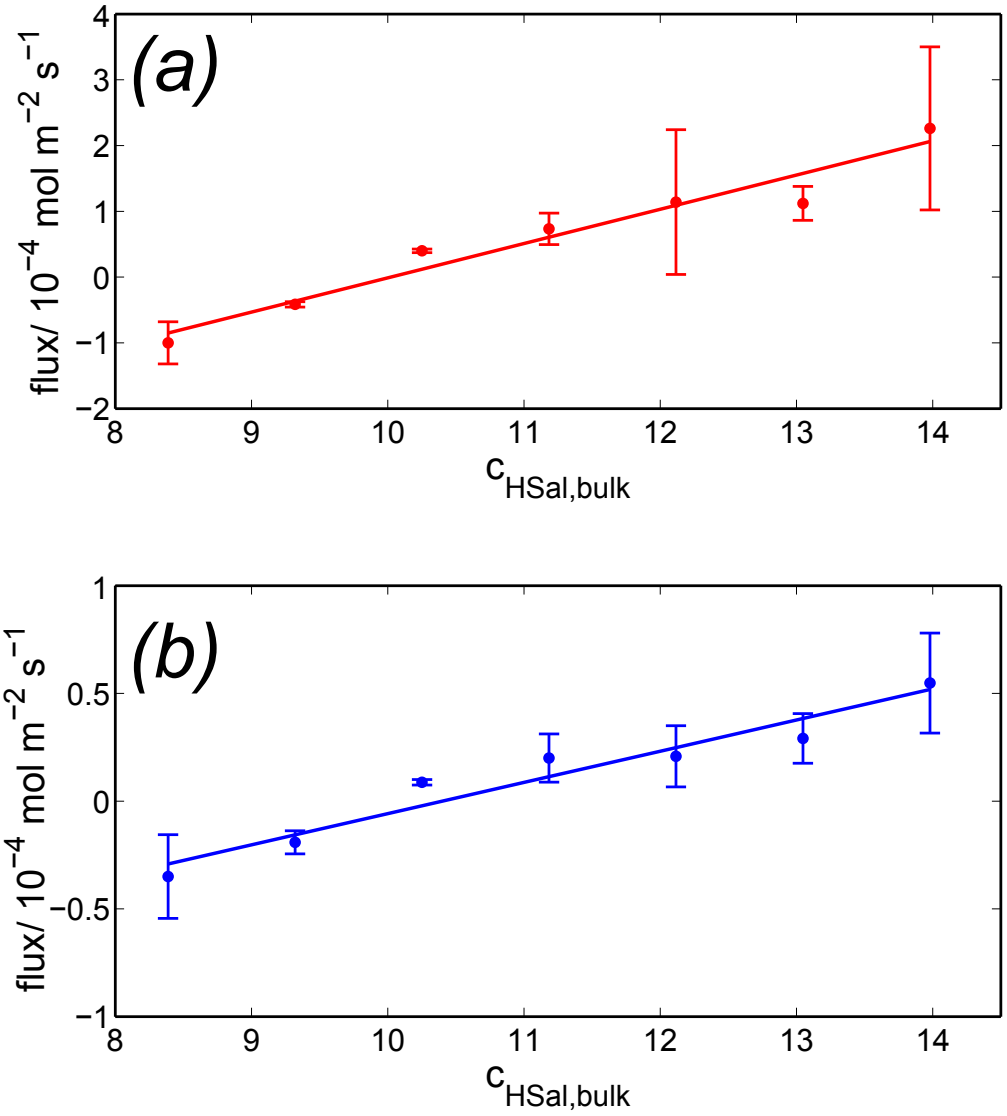

Figure 5: Plots showing how the flux per unit area into the crystal faces varies for change in bulk concentration. Data for the (001) face (a) and the ($\bar{1}$10) face (b).

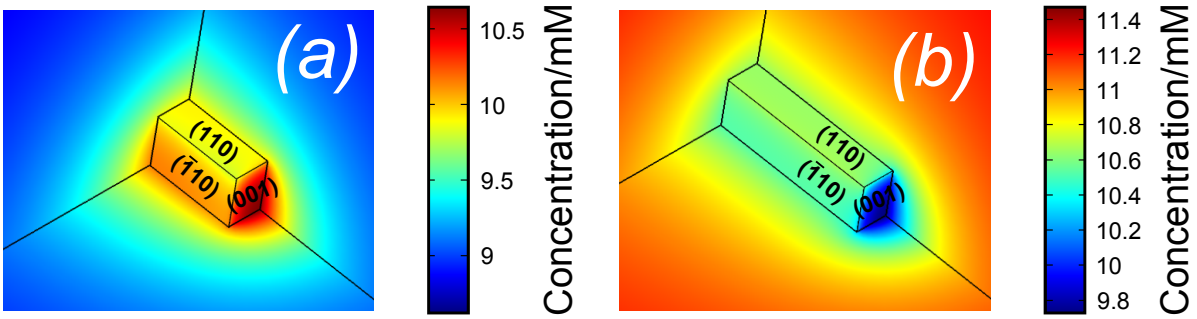

Figure 6: Examples of results of FEM simulations for dissolution in a bulk solution of 8.4 mM HSal with a crystal of largest dimension 39 μm (a) and growth in a bulk solution of 11.2 mM with a crystal of largest dimension 67 μm (b).

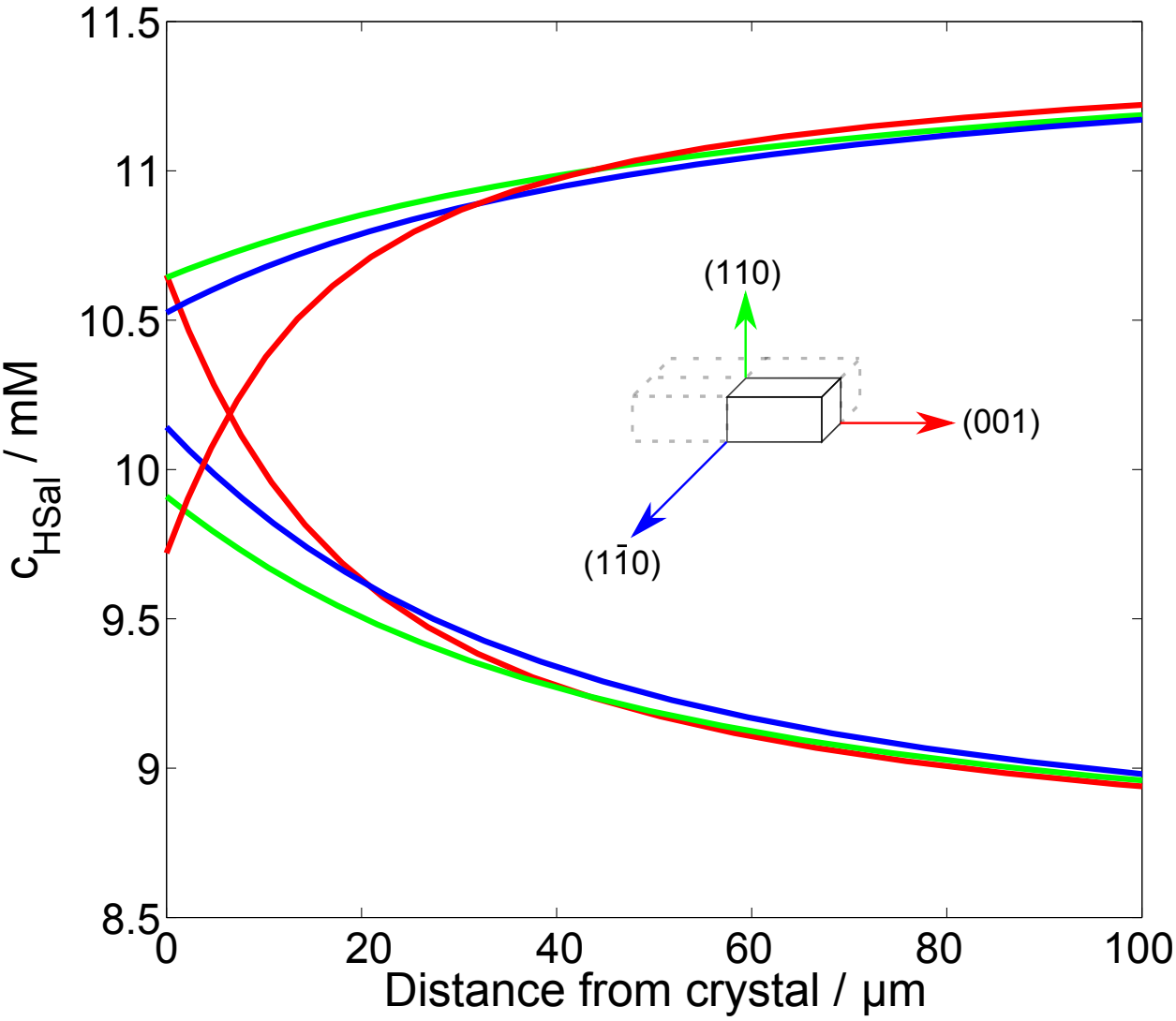

Figure 7: Plots showing the variation of concentration from the center of each face, moving perpendicularly to the bulk solution, for the case of dissolution and growth (same crystals as shown in Figure 6)

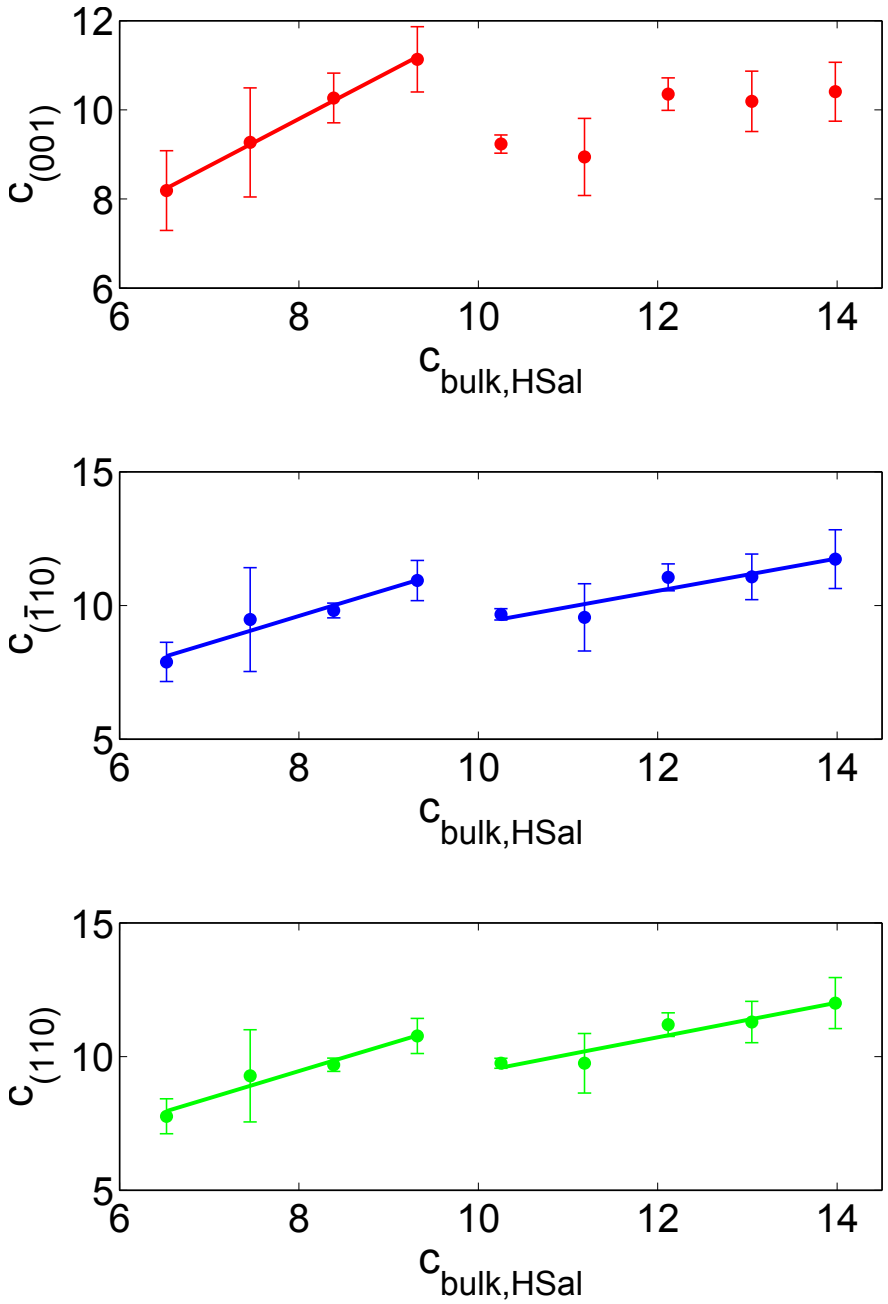

Figure 8: Plots showing how the average concentration on the surface of each face of the crystal varies with the concentration in bulk of salicylic acid (determined by MINEQL$^+$), calculated from finite element simulations such as the ones shown in Figure 6. (a) Surface concentration on the (001) face vs. bulk concentration, (b) surface concentration on the ($\bar{1}$10) face vs. bulk concentration and (c) surface concentration on the (110) face vs. bulk concentration.

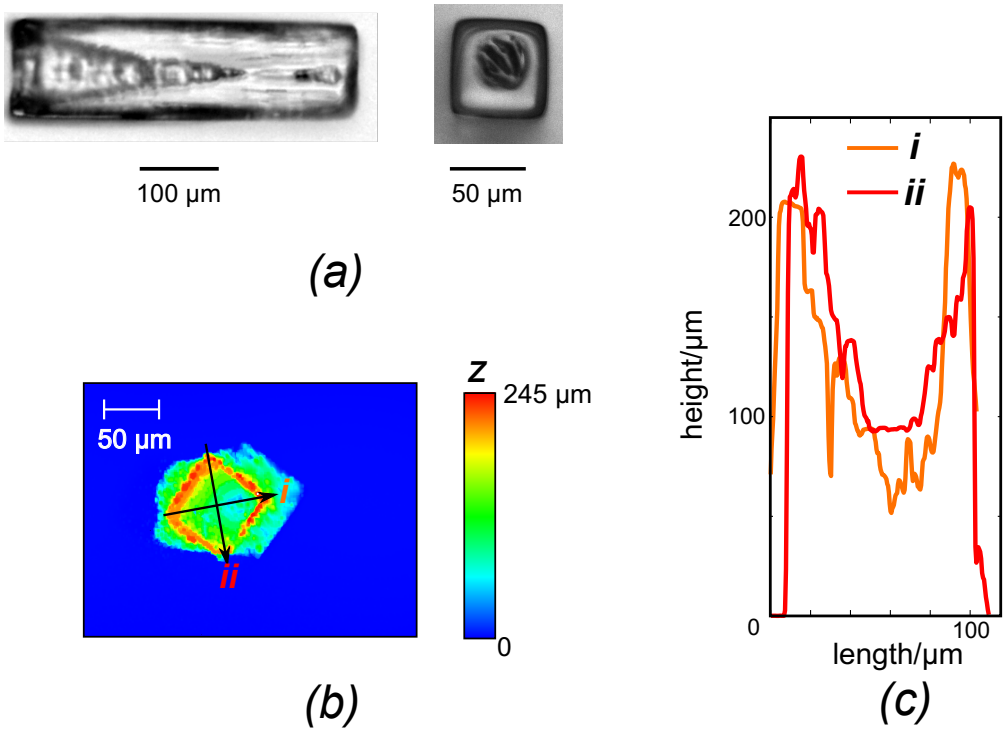

Figure 9: (a) Differential interference contrast optical microscope images of typical large salicylic acid crystals, showing hollow features in the (001) face, viewed from the side (left), and the top (right). (b) VSI image showing a hollow feature in a crystal oriented so that the (001) face was parallel with the glass surface with two cross sections of the crystal (i and ii), shown in more detail as cross-sections (c).

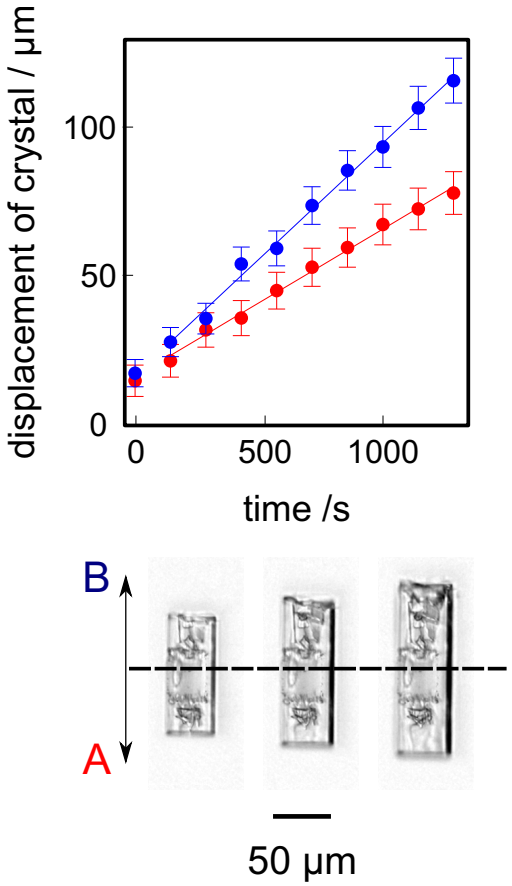

Figure 10: Plot showing the change in size of the crystal in both the A and B planes (top), from a particular reference plane illustrated by the horizontal dashed line across the time sequence images (bottom). It is observed from the time sequence images that a reasonable part of the growth in the B direction involves the existence of a hollow feature, and there is an increased growth rate compared to the other side of the crystal (A).

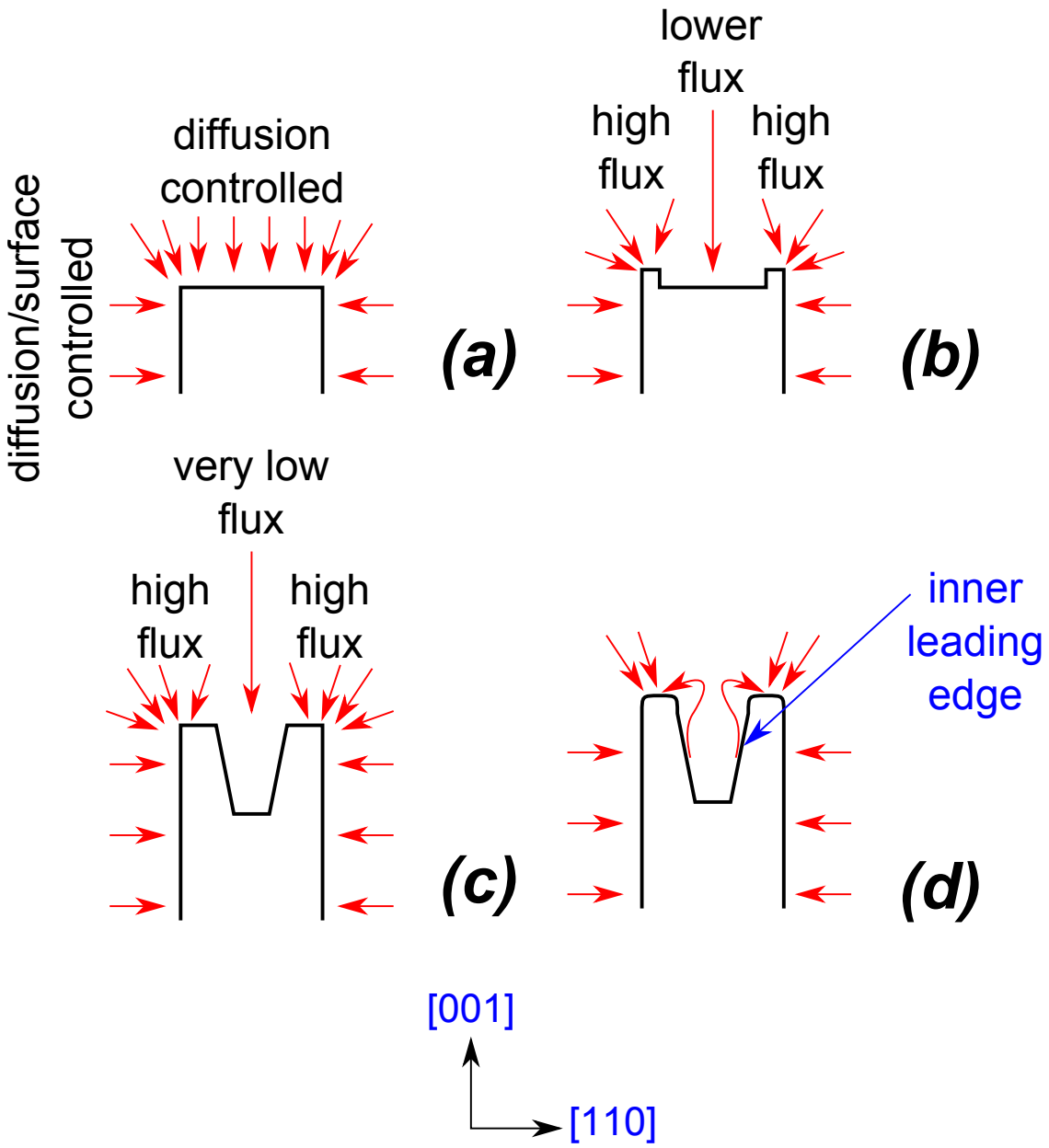

Figure 11: Illustration of the formation (a and b), growth (c) and closure (d) of hollow features on the (001) face of a salicylic acid crystal. The general flux of material is shown by the red arrows.